



## Phase distribution including a bubblelike region in supercritical fluid

Jinliang Xu <sup>1,2</sup>, Yan Wang <sup>1</sup>, and Xiaojing Ma<sup>1,\*</sup>

<sup>1</sup>Beijing Key Laboratory of Multiphase Flow and Heat Transfer for Low Grade Energy Utilization, North China Electric Power University, Beijing, 102206, China

<sup>2</sup>Key Laboratory of Power Station Energy Transfer Conversion and System, North China Electric Power University, Ministry of Education, Beijing, 102206, China



(Received 19 March 2021; revised 28 June 2021; accepted 2 July 2021; published 27 July 2021)

Pseudoboiling in supercritical fluid (SF) has been paid great attention in recent years. Available works mainly focus on thermodynamics analysis. Fewer studies were reported on the spatial time phase distribution. Here, SF is investigated in a multiphase fluid framework using molecular dynamics (MD) simulations. A simulation box contains 10 976 argon atoms, with periodic boundary conditions applied on all the box surfaces. Pressure and temperature are well controlled. Based on MD simulation results, an onset pseudoboiling temperature  $T^-$  and a termination pseudoboiling temperature  $T^+$  are defined using the neighboring molecules method, the radial distribution function method, and the two-body excess entropy method. The two transition temperatures divide the whole phase diagram into three regimes of liquidlike, two-phase-like (TPL), and gaslike, and the MD determined  $T^-$  and  $T^+$  well matched the thermodynamics-determined values. In the TPL regime, nanovoids are observed to have two distinct characteristics: (1) Particles are sparsely distributed to have gas density inside the void, but are densely populated to have liquid density outside the void. (2) Voids have a curved interface. These characteristics are very similar to bubble characteristics in subcritical pressure. Hence, voids in the supercritical state are called “bubblelike” in this paper. Nonlinear dynamics demonstrates chaotic behavior in the TPL regime, similar to the two-phase regime in the subcritical domain. The above findings give strong evidence that SF in the TPL regime consists of a mixture of bubblelike voids and surrounding liquids. Our work highlights the multiphase feature of a SF, hence, the well-established multiphase theory in subcritical pressures can be introduced to handle the complex SF.

DOI: [10.1103/PhysRevE.104.014142](https://doi.org/10.1103/PhysRevE.104.014142)

### I. INTRODUCTION

Supercritical fluids (SFs) were first discovered by Cagniard de la Tour in 1822 [1]. Such SFs have received great attention for advanced power cycles in power generation [2,3], thermochemical conversion of biomass [4,5], wastewater treatment [6], and hydrothermal synthesis of nanomaterials [7]. The large scale utilization of supercritical technologies is still far from development due to an unfavorable energy balance and challenges in separating useful products from bulk fluids [8,9]. SFs have been documented as a continuous, homogeneous, and single-phase fluid without bubbles or an interface [10]. However, the measured heat transfer significantly deviates from the predictions using single-phase fluid theory [11,12].

Pseudoboiling was initially mentioned in the literature in the 1960s to 1970s [13,14]. For forced convection heat transfer in tubes, investigators observed wall temperature overshoot before the pseudocritical point, which is similar to the critical heat flux condition in the subcritical domain [13–15]. Pseudoboiling was assumed to explain the observed phenomenon. The basic idea is that even in supercritical pressure, the second order phase change may happen, which is analo-

gized to subcritical boiling. Recently, pseudoboiling has received interest. In a series of works by Banuti’s group, pseudoboiling was analyzed using the thermodynamics approach [16,17]. An onset pseudoboiling temperature  $T^-$  and a termination pseudoboiling temperature  $T^+$  are defined based on the enthalpy analysis [16,17]. The neutron measurement technique was applied to visualize the SF structure during heating [17,18]. Together with the molecular dynamics (MD) simulations [19–21], SF is believed to have a transition between liquidlike (LL) and gaslike (GL), instead of the single-phase structure [22,23].

MD simulations have been widely applied to study SFs. Bolmatov *et al.* [24] studied the thermodynamic properties of the supercritical state and found that the specific heat has a crossover between the LL and GL regimes. Gallo *et al.* [19] studied the thermodynamic properties of water in the supercritical region and found that the lines connecting the maxima of the response functions converge when approaching the critical point in a single line, called the Widom line. They further showed that the Widom line coincides with the crossover from LL to GL behavior, which is clearly visible in the transport properties. The transition between the two regimes when crossing the Widom line was experimentally demonstrated using x-ray scattering [20]. Raju *et al.* [25] shows that in the supercritical regime, a mutually miscible binary mixture experiences a transition between LL and GL

\*mxj@ncepu.edu.cn

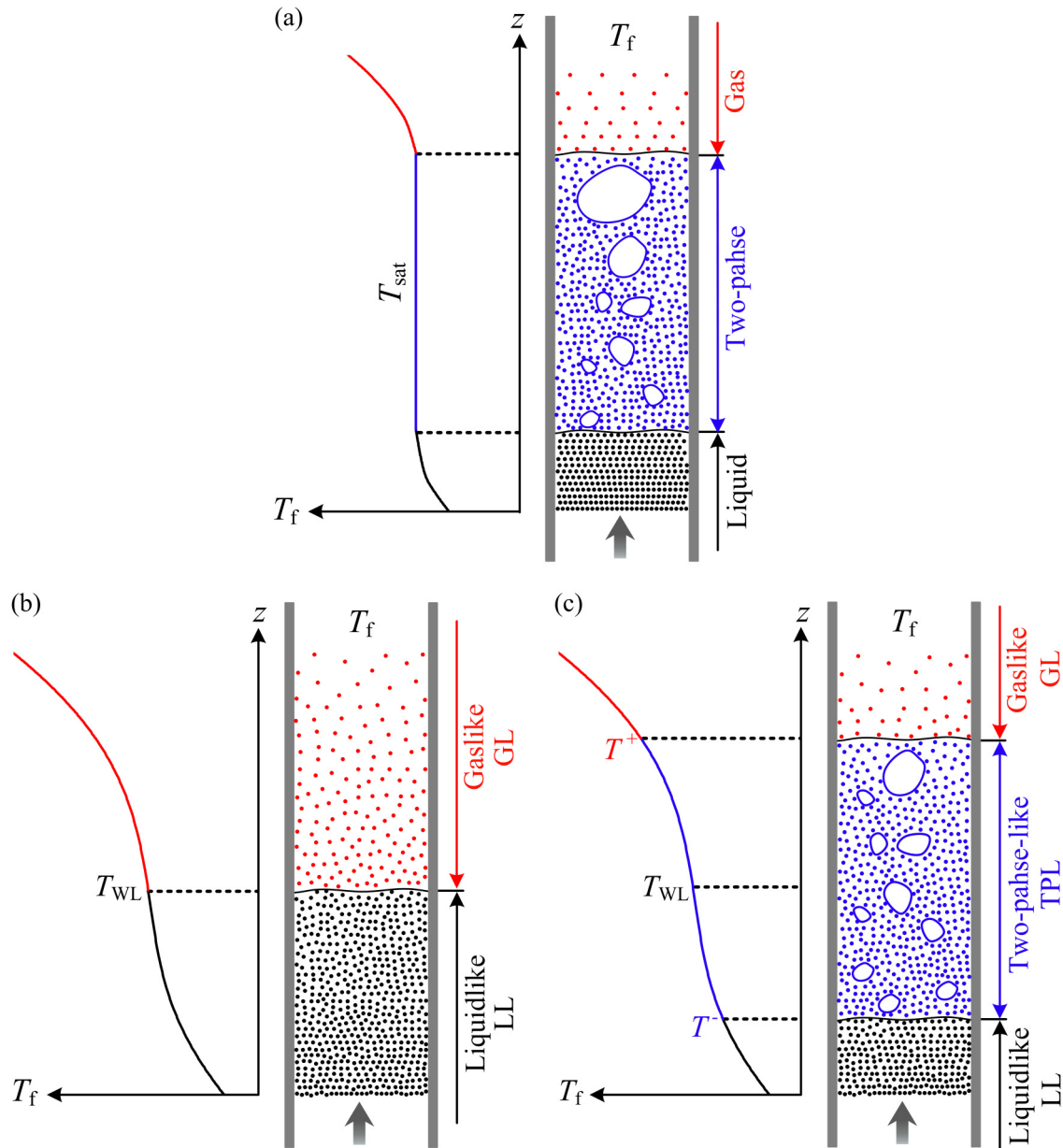


FIG. 1. Well-defined heat transfer problem in ultralong tubes at equilibrium state. (a) Subcritical fluid contains three regimes of liquid, two phase, and gas, in which the two-phase regime occurs at a constant saturation temperature  $T_{sat}$ , containing spherical or deformable bubbles with liquid-gas interface. (b) Current cognition on SF shows sharp transition from LL to GL when crossing a temperature  $T_{WL}$  at the Widom line. (c) By crossing two transition temperatures,  $T^-$  and  $T^+$ , SF contains three regimes of LL, TPL, and GL. We use different approaches to determine  $T^-$  and  $T^+$ , and find a bubblelike regime.

across a single Widom line, but two Widom lines are present in the supercritical regime for an immiscible binary mixture.

Classically, bubbles can exist in subcritical pressures but cannot exist in supercritical pressures [see Figs. 1(a) and 1(b)]. When crossing the Widom line, heat added to the SF can be divided into two parts. One is for the temperature rise and the other is to overcome intermolecular attraction to separate neighboring molecules, which forms the theoretical basis for pseudoboiling and is clarified as the second order phase change [16]. Hence, we propose the three-regime model by adding the two-phase-like (TPL) regime [see Fig. 1(c)]. Two important issues need to be solved for pseudoboiling. The

first is to quantitatively determine the two transition temperatures, and the second is to answer the question of whether bubbles exist in a SF. For the first issue, Banuti [16] stated that supercritical state transitions require energy to increase the temperature. Thus, a new equation for the Widom or pseudoboiling line was given. Recently, Ha *et al.* [26] determined two transition boundaries instead of the single Widom line to divide the entire  $P$ - $T$  phase diagram into three zones using the machine learning technique. The second issue is to find what the phase distribution is in the TPL regime. In fact, available studies indicate a bubblelike phase for pressure slightly larger than the critical pressure [27,28]. However, a

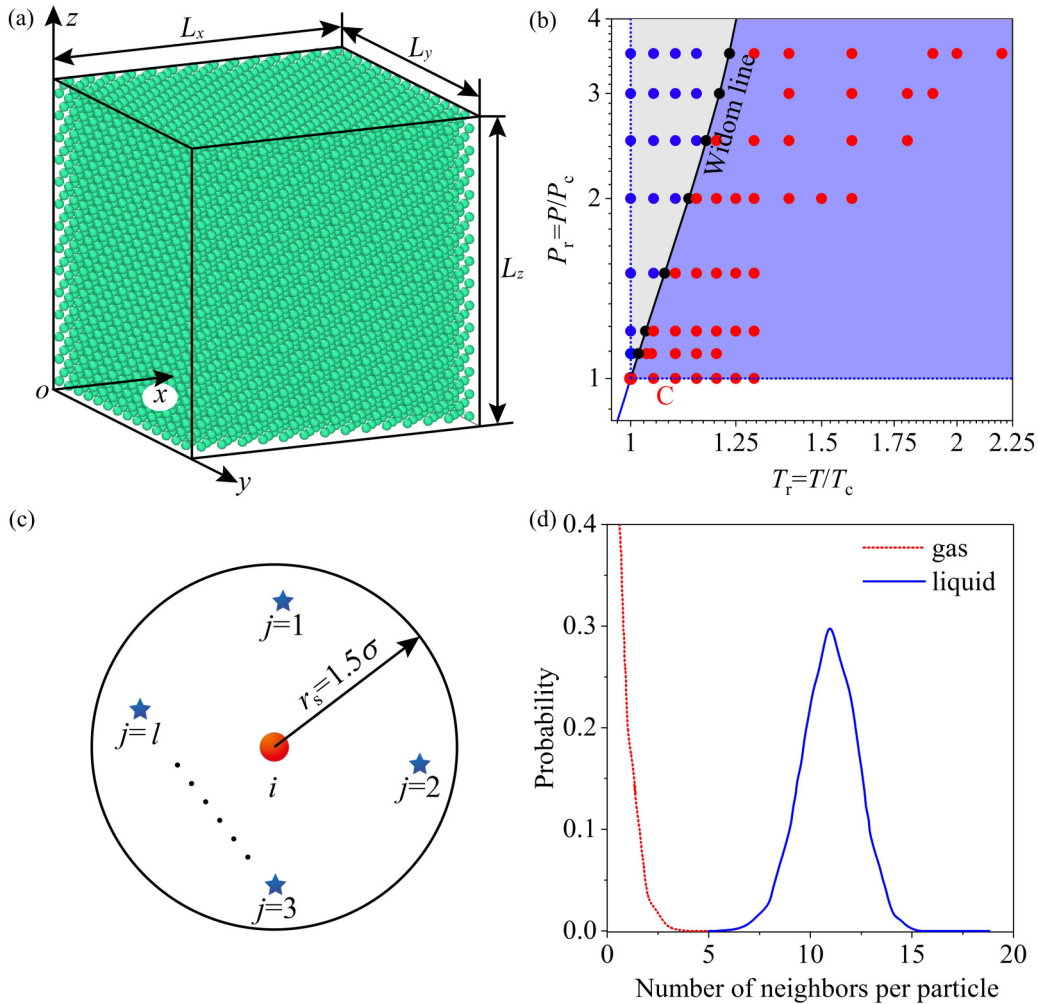


FIG. 2. Molecular dynamics simulations of supercritical argon. (a) Simulation cubic box of  $L_x = L_y = L_z$  is set to contain 10 976 atoms for all considered cases. Periodic boundary conditions are applied along the  $x$ ,  $y$ , and  $z$  coordinates. The box size may differ at various pressures. The face centered cubic (fcc) structure is initially assumed but will evolve when the simulation begins. (b) Data points are shown on the  $P_r$ - $T_r$  phase diagram, where  $P_r = P/P_c$  and  $T_r = T/T_c$  are the reduced pressure and temperature, respectively. The Widom line is determined based on the maximum specific heat at various supercritical pressures. (c) The molecule marking method refers to a molecule being marked as a liquid molecule if it has at least five neighboring molecules within a distance of  $r_s = 1.5\sigma$ ; otherwise, it is marked as gas. (d) Probability distribution of liquid and gas dependent on the number of neighboring molecules at the coexistence point [38].

bubblelike phase was never reported for pressures far above the critical pressure.

Here, we start with MD simulations of argon. Such fluid has been widely used as a model fluid in MD simulations. Great attention was paid to the multiphase characteristic. Three different approaches, the neighboring molecules method, the radial distribution function (RDF) method, and the two-body excess entropy method, were applied to determine the two transition temperatures, matching the thermodynamics-determined values. The bubblelike structure was observed and explained. The bubblelike structure is not found in the LL and GL regimes, but it does appear for temperatures larger than  $T^-$  but smaller than  $T^+$ . Non-linear analysis was performed using the time series density fluctuations. We show that both the LL and GL regimes behave with random characteristics. However, the TPL regime displays chaotic behavior, which is similar to the nonlinear characteristic of two-phase fluid in subcritical pressure. Our

work highlights the multiphase feature including bubblelike structure in SF.

## II. METHODS AND SIMULATIONS

### A. Computation domain, method, and data process

Figure 2(a) shows the computation domain, where  $x$ ,  $y$ ,  $z$  are the three-dimensional coordinates. Molecular dynamics (MD) simulations were performed in a cubic box containing 10 976 argon atoms, resulting in better control of the thermodynamic state of pressure and temperature and improved statistical averaged parameters. The 10 976 particles were also used in Refs. [29,30]. The cubic box has the size of  $L_x = L_y = L_z = L$ , determined by the average density of fluid deduced from pressure  $P$  and temperature  $T$ . Periodic boundary conditions are applied on the six box surfaces. For MD simulations,  $L_x$ ,  $L_y$ , and  $L_z$  should be larger than the cutoff distance, which is  $\sim 5.8\sigma$  for argon [31,32]. This size criterion is well satisfied

in this paper; for example,  $L_x = L_y = L_z = 32.5331\sigma$  at  $P_c = 4.863$  MPa and  $T_c = 150.69$  K, where “c” refers to the critical condition. Initially, the argon atoms are assumed to have face centered cubic (fcc) structure, but with time evolution such configuration will be melting to form different fluid structures, which are interest in this paper. MD simulations covered the following data ranges of  $P = (1.0\text{--}3.5)P_c$  and  $(1.0\text{--}2.2)T_c$ . At each  $P$ , different runs are scanned with a continuous increase of  $T$  [see Fig. 2(b) for the simulation runs in the  $P$ - $T$  phase diagram]. The density  $\rho$  is defined as the number of particles ( $N$ ) in a fluid volume ( $V = L^3$ ):  $\rho = N/L^3$ , which is treated as a target control parameter. The size of the simulation box can be determined based on  $\rho$  and  $N$  as  $L = (N/\rho)^{1/3}$ , where  $N = 10976$  in this paper. Because different densities are treated in this paper, our calculations need to update the simulation box size for different runs. In one word, density is controlled in the target value via controlling the simulation box size.

For the argon molecule, the Newton equation is written as

$$m \frac{d\vec{r}^2}{dt^2} = \sum_{j \neq i, j=1}^N \vec{F}_{ij} + \vec{F}_{\text{ex}}. \quad (1)$$

The first term of the right side of Eq. (1) represents the force between argon atoms, where  $m$  is the argon atom mass, and  $r$  is the distance between atom  $i$  and atom  $j$ . Because there is no external force in this study,  $\vec{F}_{\text{ex}} = 0$ . The intermolecular force is related to the potential as

$$F_{ij} = -\frac{\partial \phi_{ij}}{\partial r_{ij}}. \quad (2)$$

The Lennard Jones (LJ) potential for argon is written as [33]

$$\phi(r) = 4\epsilon \left[ \left( \frac{\sigma}{r} \right)^{12} - \left( \frac{\sigma}{r} \right)^6 \right], \quad (3)$$

where  $\epsilon$  is the energy scale and  $\sigma$  is the length scale, which are  $\epsilon = 1.67 \times 10^{-21}$  J and  $\sigma = 3.405 \times 10^{-10}$  m.

The velocity Verlet method is used to integrate the momentum equation and the cell subdivision technique is applied to improve the computational efficiency. The position  $\mathbf{r}(t + \Delta t)$ , velocity  $\mathbf{v}(t + \Delta t)$ , and  $\mathbf{a}(t + \Delta t)$ , at the time  $t + \Delta t$  are updated based on the values at the previous time  $t$  [34].

$$\mathbf{r}(t + \Delta t) = \mathbf{r}(t) + \mathbf{v}(t)\Delta t + \frac{1}{2}\mathbf{a}(t)\Delta t^2, \quad (4)$$

$$\mathbf{v}(t + \Delta t) = \mathbf{v}(t) + \frac{1}{2}[\mathbf{a}(t) + \mathbf{a}(t + \Delta t)]\Delta t, \quad (5)$$

where  $\Delta t$  is the time step which is  $\Delta t = 0.00046\tau$  corresponding to 1 fs;  $\tau = \sqrt{m\sigma^2/\epsilon} = 2.16 \times 10^{-12}$  s is the time scale. In this study,  $NVT$  is used for MD simulations. The reason why we choose  $NVT$  instead of  $NPT$  is explained in Sec. III. At each pressure, the fluid temperature is well controlled by the Nosé-Hoover method [35,36]. A total of 6 000 000 time steps are calculated for each run. The first 1 000 000 steps are regarded as the transition from the initial fcc structure to the steady oscillation stage. Various statistical parameters are achieved for the latter 5 000 000 steps. The simulation is conducted using the open source large scale atomic/molecular massively parallel simulator (LAMMPS) [37]. The OVITO software is used for the atomic visualization.

TABLE I. The nondimensional parameters.

Property	Parameters
Length	$r^* = \frac{r}{\sigma}$
Time	$t^* = \frac{t}{\tau}$
Force	$F^* = \frac{F\sigma}{\epsilon}$
Temperature	$T^* = \frac{k_B T}{\epsilon}$
Velocity	$v^* = \frac{v\tau}{\sigma}$
Density	$\rho^* = \frac{\rho\sigma^3}{m}$
Energy	$\text{Pe}^* = \frac{\text{Pe}}{\epsilon}$

In order to perform the transient and nonlinear analysis of local fluid densities, we select the centered  $10\sigma$  thickness in the  $y$  direction over the  $xz$  plane as a slice to obtain the statistical density in such a slice at  $t$ . The nondimensional particle density is

$$\rho_{lo}\sigma^3 = \frac{\sigma^3}{A\Delta y(J_{\text{Start}} - J_{\text{End}} + 1)} \sum_{J_{\text{Start}}}^{J_{\text{End}}} N_{lo}, \quad (6)$$

where  $J_{\text{Start}}$  and  $J_{\text{End}}$  are the start and end time step of the statistics,  $A$  is the  $xz$  plane area ( $A = L_x L_z$ ),  $\Delta y = 10\sigma$ , and  $N_{lo}$  is the total number of molecules in the slice. Because  $N_{lo}$  is changed versus time, the fluid density varies with time, indicating the mass exchange between the selected slice and the nearby fluid volumes. In order to present results in a general sense, computations are performed using a set of nondimensional parameters, which are expressed in Table I. All the parameters are scaled by  $m$ ,  $\sigma$ , and  $\epsilon$  of argon atoms.

The Ten Wolde and Frenkel (TWF) method is applied to mark the target molecule as a liquid molecule or gas molecule [38,39]. If there are at least five molecules except for the target molecule in such a sphere, the target molecule is marked as a liquid molecule; otherwise, it is marked as a gas molecule [see Fig. 2(c)]. Hence, all molecules are marked as either a liquid molecule or a gas molecule. We define the vapor mass quality as  $\chi_{\text{gas}} = N_{\text{gas}}/N$ , where  $N_{\text{gas}}$  and  $N$  are the number of gas molecules and the total number of molecules in the box, respectively. Figure 2(d) shows the probability distribution when using different neighboring molecules of the target molecule, which will be analyzed in Sec. III B.

The radial distribution function (RDF), which is given as  $g(r_c)$ , characterizes the local density fluctuations with a distance  $r_c$  from the center of a specific atom or molecule [40],

$$g(r_c) = \frac{1}{\rho_{\text{ave}} 4\pi r_c^2 \delta r_c} \frac{\sum_{i=1}^{N_t} \sum_{j=1}^N \Delta N(r_c \rightarrow r_c + \delta r_c)}{N N_t}, \quad (7)$$

where  $N_t$  is the total steps for the integration;  $\Delta N$  is the number of particles for a size interval from  $r_c$  to  $r_c + \delta r_c$ . The  $g(r_c)$  approaches 1 when  $r_c$  is large.

Previous studies have shown a strong connection between the degree of ordering, the transport properties of fluids, and their excess entropy [41]. The excess entropy is defined as the entropy of the fluid relative to that of the ideal gas at the same



temperature and pressure, and is expressed as

$$s^{\text{ex}} = s - s_{\text{id}}, \quad (8)$$

where  $s$  is the total entropy,  $s_{\text{id}}$  is the ideal gas entropy, and  $s^{\text{ex}}$  can be expressed based on the expansion of  $n$ -body correlation functions, which is often approximated by the first term, namely, the two-body contribution on excess entropy  $s^{(2)}$ . Indeed, for the LJ system, this two-body contribution to the entropy is between 85% and 95% over a fairly wide range of densities [31]. The  $s^{\text{ex}}$  can be estimated from the two-body contribution on the excess entropy  $s^{(2)}$  based on  $g(r_c)$  as [41]

$$s^{(2)} = -2\pi\rho_{\text{ave}}k_B \int [g(r_c) \ln g(r_c) - g(r_c) + 1]r_c^2 dr_c, \quad (9)$$

where  $k_B$  is Boltzmann's constant. As  $s^{(2)}$  is related to  $g(r_c)$ , it can be used to characterize the degree of ordering for a fluid. Since  $s^{(2)}$  equals zero for completely disordered systems (i.e., the ideal gas), but becomes large and negative for ordered structures ( $s^{(2)} \rightarrow -\infty$  for perfect crystalline arrangements), it provides a method to characterize the degree of disordering in a system [42]. The scaled two-body excess entropy  $\ln[-s^{(2)}/k_B]$  is used in this paper.

### B. Thermodynamically determined transition temperatures for pseudoboiling

Section II A involves the details of MD simulation and the data process, which form the basis to generate the three methods of neighboring molecules, radial distribution function, and two-body excess entropy, yielding the transition boundaries for different phase distribution of LL, GL, and TPL, which are further discussed in the Results and Discussion. The transition boundaries determined by the three methods are compared with the thermodynamically determined values.

Banuti [16] used enthalpy asymptotes for the ideal gas  $i_g$  and liquid  $i_l$  reference states to evaluate the temperature intervals for supercritical phase change. Pseudoboiling enthalpy is recorded as the enthalpy difference between  $T^+$  and  $T^-$ . As seen in Fig. 3, the two blue lines represent enthalpy lines for the ideal gas and liquid, where  $i$  is the enthalpy of the fluid. The enthalpy curves of argon at pressures of  $1.1P_c$ ,  $1.5P_c$ , and  $2.0P_c$  consist of a curved  $CD$  part and two parts beyond the  $CD$  section. The former includes a pseudoboiling point (pb), in which the temperature and enthalpy are recorded as  $T_{\text{pb}}$  and  $i_{\text{pb}}$ , respectively. The red line  $AB$  is the tangent line that passes through the pb. The two points of  $A$  and  $B$  can be precisely determined by crossing the tangent line with the two enthalpy lines of the ideal liquid and gas. In this way, the onset pseudoboiling temperature  $T^-$  is located at point  $A$ , while the termination pseudoboiling temperature  $T^+$  is at point  $B$ . Correspondingly, the points  $C$  and  $D$  are marked on the enthalpy curve of the supercritical fluid defined at the two temperatures of  $T^-$  and  $T^+$ , respectively.

### C. Nonlinear analysis of fluids

Multiphase flow in subcritical pressure behaves with a strong nonlinear characteristic. Thus, nonlinear analysis has been widely applied for phase change heat transfer [43,44]. The outcomes of nonlinear analysis help us to understand

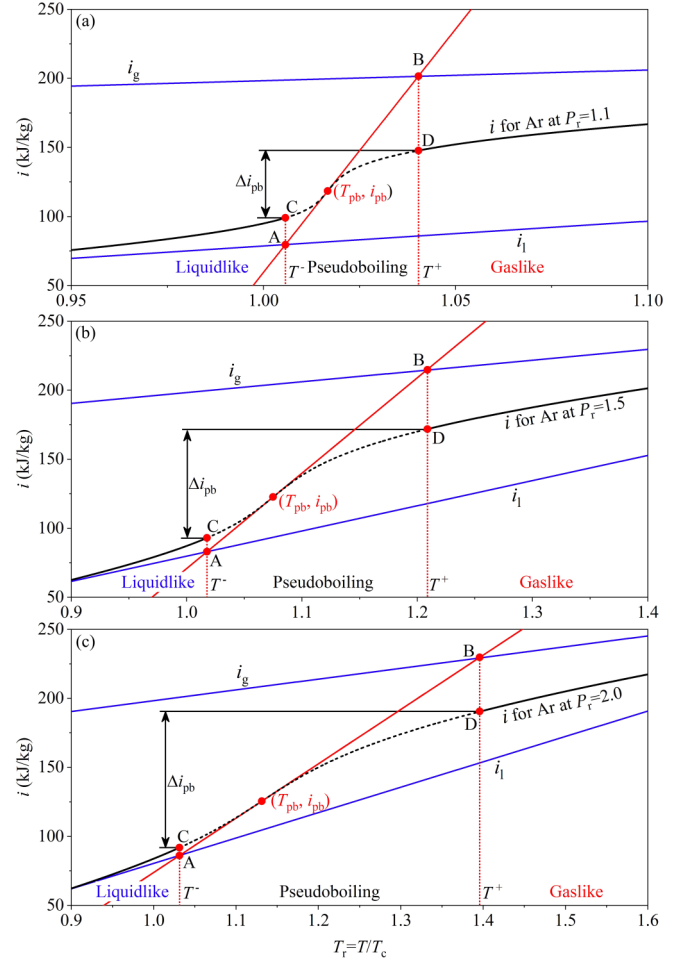


FIG. 3. The  $i$ - $T_r$  curves across the pseudocritical point to define the transition temperatures of  $T^-$  and  $T^+$ . (a)  $P_r = 1.1P_c$ , (b)  $P_r = 1.5$ , and (c)  $P_r = 2.0$ . This method is also called the thermodynamically determined method [16].

the complicated mass, momentum, and energy interaction between the vapor phase and liquid phase. A major contribution of the present paper is to demonstrate the multiphase feature for supercritical fluids. Hence, it is necessary to introduce the nonlinear analysis to understand the complicated fluid in supercritical pressure.

Nonlinear dynamics was introduced to analyze the transient densities in the center slice of  $10\sigma$ . The behavior of a nonlinear system can be analyzed based on the trajectories of attractors in the phase space. Therefore, the multidimensional phase space portraits can be reconstructed from the time series of density fluctuations over the entire cubic box. The time series density signal  $X$ , as obtained from the simulations, is digitized with the time step  $\Delta t$  for the resultant  $(n+1)$  signal values. The vector time series is defined as  $\{X(t), X(t+\tau_D), X(t+2\tau_D), \dots, X(t+(n-1)\tau_D)\}$ , where  $n$  is the embedded dimension and  $\tau_D$  is the time delay. The dynamic properties of a system can be studied by reconstructing the phase space if  $n \geq 2D+1$ , where  $D$  is the fractal dimension of the system [45].

To reasonably reconstruct the phase space, careful attention is given to the choice of the embedding dimension  $n$  and delay

time  $\tau_D$ . If  $\tau_D$  is too small, the attractor becomes flattened, making the analysis impossible. Alternatively, if  $\tau_D$  is too large, the attractor becomes too complex and outputs incorrect information on the dynamic behavior of the system. Several methods, such as time delay, mutual information, autocorrelation, and C-C, could determine a suitable time delay [46]. C-C method is a simpler method for estimating  $\tau_D$  using the correlation integral. Here, the proper value of  $\tau_D$  is determined by the C-C method.

For nonlinear analyses, the correlation dimension is the most widely used approach to estimate the fractal dimensions of an attractor. The correlation dimension  $D_2$  can be decided from the power law relationship between the correlation integral of an attractor and the neighborhood radius of the analysis hypersphere [45,47]:

$$D_2 = \lim_{r_d \rightarrow 0} \frac{\ln C(r_d)}{\ln r_d}, \quad (10)$$

where  $C(r_d)$  is the correlation integral defined as  $C(r_d) = \frac{2}{N_d(N_d-1)} \sum_{j=1}^{N_d} \sum_{i=j+1}^{N_d} \theta(r_d - |\vec{x}_i - \vec{x}_j|)$ ,  $x_i$  are the points on the attractor, and  $N_d$  is the number of embedding points in the phase space. The correlation integral is a measure of the number of points within a neighborhood of radius  $r_d$  as averaged over the entire attractor. The  $\theta(x)$  is the Heaviside step function of

$$\theta(x) = \begin{cases} 0 & x \leq 0 \\ 1 & x > 0 \end{cases}. \quad (11)$$

Usually,  $D_2$  is determined by calculating the slope of the fitting curve crossing the middle scale region of  $\ln C(r_d)$  versus  $\ln r_d$ . If  $N_d$  in the denominator is significant, the  $D_2$  for a chaotic system converges with an increased embedding dimension  $n$ . In contrast,  $D_2$  for a random system increases with an increased embedding dimension  $n$ .

### III. RESULTS AND DISCUSSION

#### A. Model validation

It is noted that both  $NVT$  and  $NPT$  are used in MD simulations. For  $NVT$ , volume and temperature are controlled to target values. Instead, for  $NPT$ , pressure and temperature are controlled. For both methods of  $NVT$  and  $NPT$ , oscillating of any parameter is unavoidable. Allen and Tildesley [48] pointed out that oscillations of various parameters are weaker for  $NVT$  than those for  $NPT$ . Skarmoutsos and Samios [49] commented on the fact that  $NPT$  creates oscillation of the system volume, which is not suitable for spatial time density analysis, but the density analysis can be conveniently performed using  $NVT$ .

Based on the control strategy of  $NVT$ ,  $k_B T/\varepsilon$ ,  $P\sigma^3/\varepsilon$ , and  $Pe/\varepsilon$  are plotted in Fig. 4(a), including three regimes of an initial stage within  $0 \text{ ps} < t < 3 \text{ ps}$ , a transition stage within  $3 \text{ ps} < t < 100 \text{ ps}$ , and an equilibrium stage for  $t > 100 \text{ ps}$ . At the initial time of  $t = 0$ , all the fluid atoms are assumed to have the fcc structure with zero velocities. Hence, the system temperature is zero at  $t = 0$ . Following  $t > 0$ , intermolecular forces are applied on each atom based on Eq. (1) to achieve kinetic energy. Hence, the system temperature is small, on the magnitude of  $(10^{-14} - 10^{-10})k_B T/\varepsilon$ , but not zero within

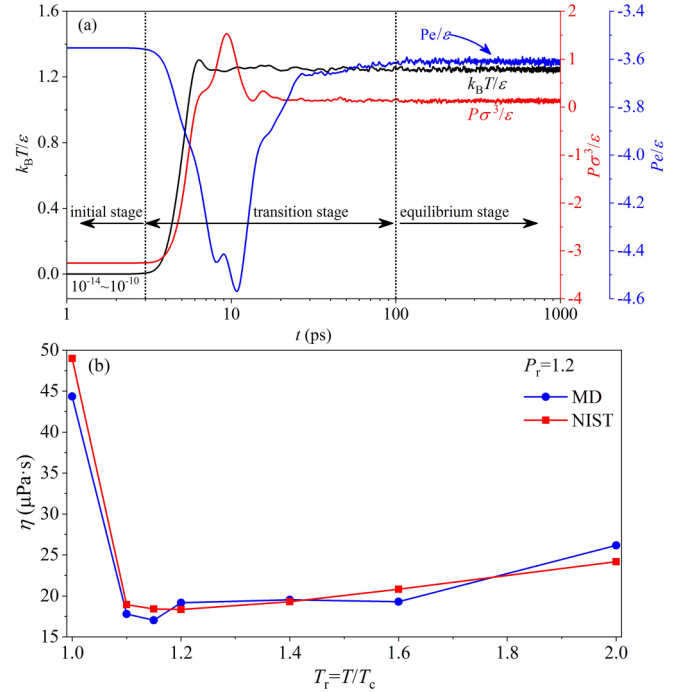


FIG. 4. Validation of MD simulation results: (a) variations of various parameters versus time; (b) comparison of MD results with those coming from NIST software.

the initial stage. We note that the characteristic time of argon molecules is  $\tau = \sqrt{m\sigma^2/\varepsilon} = 2.16 \text{ ps}$ , matching the time duration of  $\sim 3 \text{ ps}$  for the initial stage. Thus, the relaxation time for the Nosé-Hoover thermostat temperature control is  $\sim 1\tau$ . Following the initial stage, the system switches to the transition stage and the system temperature sharply increases and is stabilized at the target value.

In order to characterize the oscillation characteristic in the steady stage, standard deviation between average value and instantaneous value of any parameter is [50]

$$e_k = \left\{ \left[ \sum_1^k (e - e_R)^2 \right] / (k - 1) \right\}^{0.5} \times 100\%, \quad (12)$$

where  $e$  refers to the deviation,  $e_R$  means the average deviation, and  $k$  is the number of data samples. For temperature  $T$  in the period of 100–1000 ps, the computation outcomes give the average value of 1.246 for  $k_B T/\varepsilon$ , exactly matching the setting value.  $e_k$  equals 0.77% in this period, meaning very small oscillation due to the controlled temperature using the Nosé-Hoover method. Other parameters show similar behavior. Thus, the time period for  $t > 1000 \text{ ps}$  is used for the data analysis in this study.

Another issue is to verify that our MD simulation results are correct. In order to do so, we compared the simulated physical properties of argon with those coming from the NIST software [see Fig. 4(b)]. The latter has sufficient accuracy for engineering applications. Viscosity is selected as an example physical property to be compared. The pressure is chosen as  $1.2P_c$  but the temperature is increased from  $T_c$  to  $2.0T_c$ . It is seen that our simulation results agree well with the values coming from the NIST software.

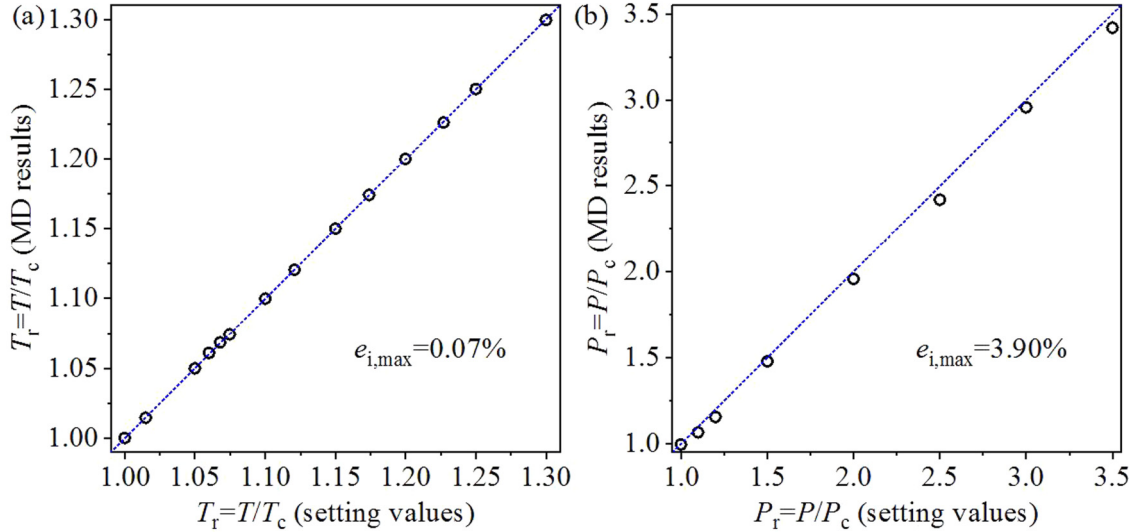


FIG. 5. Comparison between setting values and final computed values (a) for reduced temperature and (b) for reduced pressure.

In our simulation, the setting parameters are temperature and density, but density is dependent on the setting pressure and temperature. During the simulation, the temperature is well controlled to be the setting value, with the maximum deviation between the setting value and the final averaged value less than 0.07% [see Fig. 5(a)]. Hence, the following results are plotted using the setting temperature. However, the computed pressures are oscillating during simulation with the maximum deviation less than 3.90% [see Fig. 5(b)]. Hence, the following results are presented using the final calculated pressure, instead of the setting pressure.

### B. Transition boundaries determined by neighboring molecules method

In this section, we show the transition boundaries among the three regimes of LL, GL, and TPL using the neighboring molecules method. Figure 2(c) presents a  $1.5\sigma$  radius sphere encircling a target molecule and its neighboring molecules (marked as  $j = 1, 2, \dots, l$ ), where  $n$  is the maximum number of molecules that can be included in the sphere except the target molecule. Actually, the neighboring molecules method is a statistical method. As seen from Fig. 2(d), the target molecule has the largest probability to be a gas molecule if  $l < 5$ , but has the largest probability to be a liquid molecule if  $l \geq 5$ . This method is recommended by Wedekind and Reguera [51] and Losey and Sadus [39], and is also used here.

For multiphase flow in subcritical pressure, vapor mass quality ( $\chi_{\text{gas}}$ ), characterizing the vapor mass relative to the total mass for a specific two-phase mixture, is an important parameter to influence various performance parameters such as pressure drop and heat transfer coefficient [52]. Here, we try to provide a similarity between subcritical pressure and supercritical pressure. Therefore, we define the vapor mass quality as  $\chi_{\text{gas}} = N_{\text{gas}}/N$ , where  $N_{\text{gas}}$  and  $N$  are the number of gas molecules and the total number of molecules in the box, respectively. The vapor mass quality increases with temperatures for a given pressure but decreases with pressure for a given temperature, as seen in Fig. 6(a). Under subcritical

pressures, fluids are regarded as a liquid if  $\rho > 0.9\rho_{\text{sat},l}$  and as a gas if  $\rho < 0.1\rho_{\text{sat},l}$ , where  $\rho_{\text{sat},l}$  is the saturation density of the liquid. This is called the 10%–90% method [53]. This method is extended to the supercritical pressure to classify SFs into LL, TPL, and GL with  $\chi_{\text{gas}} < 0.1$ ,  $0.1 < \chi_{\text{gas}} < 0.9$ , and  $\chi_{\text{gas}} > 0.9$ , respectively. Two transition temperatures of  $T^-$  and  $T^+$  are defined at the crossing points between the vapor mass quality curve and the criteria of  $\chi_{\text{gas}} = 0.1$  and  $\chi_{\text{gas}} = 0.9$ , as seen in Fig. 6(a). The two transition boundaries divide the entire space into the three regimes of LL, TPL, and GL, which is called the neighboring molecules method, as seen in Fig. 6(b).

At the critical point with  $P_r = 0.995$  and  $T_r = 1$ , the coexistence of liquid and gas molecules is observed to show the TPL behavior, as seen in Fig. 6(c) (see Supplemental Material [54] for videos corresponding to figures in text). Liquid molecules are populated together with a curved interface that is opposite to the gas molecule cluster in a three-dimensional (3D) manner. The TPL structure at the critical point is sensitive to variations in the temperature. The system is switched from TPL to GL at  $1.05T_c$ , in which more than 90% of molecules are yellow, as seen in Fig. 6(d) (see Supplemental Material [54] for 3D movie). At the sufficiently high pressure of  $2.419P_c$ , the LL, TPL, and GL appear consecutively at temperatures of  $T_c$ ,  $1.17T_c$ , and  $1.7T_c$ ; see snapshots in Figs. 6(e)–6(g) (see Supplemental Material [54] for 3D movie). In summary, previous studies show that SFs are either LL or GL, while TPL is not observed for pressures far above the critical pressure [22]. Here, we determine the temperature interval to contain TPL including the coexistence of liquidlike and gaslike regimes, which is presented later.

It is noted that the computation outcomes may be dependent on the setting  $l$  value (see Fig. 7). Even though there exists a difference between  $l = 5$  and  $6$ , the major finding and conclusion are the same for different  $l$ . Here, the  $l = 5$  is applied, which is also used by other investigators [38,39]. Based on the  $T^-$  and  $T^+$  in Figs. 6(a) and 6(b), we show that argon exhibits a LL regime with  $\rho\sigma^3 > 0.4956 \pm 0.004$  and a GL regime with  $\rho\sigma^3 < 0.1755 \pm 0.01$ , while the TPL regime



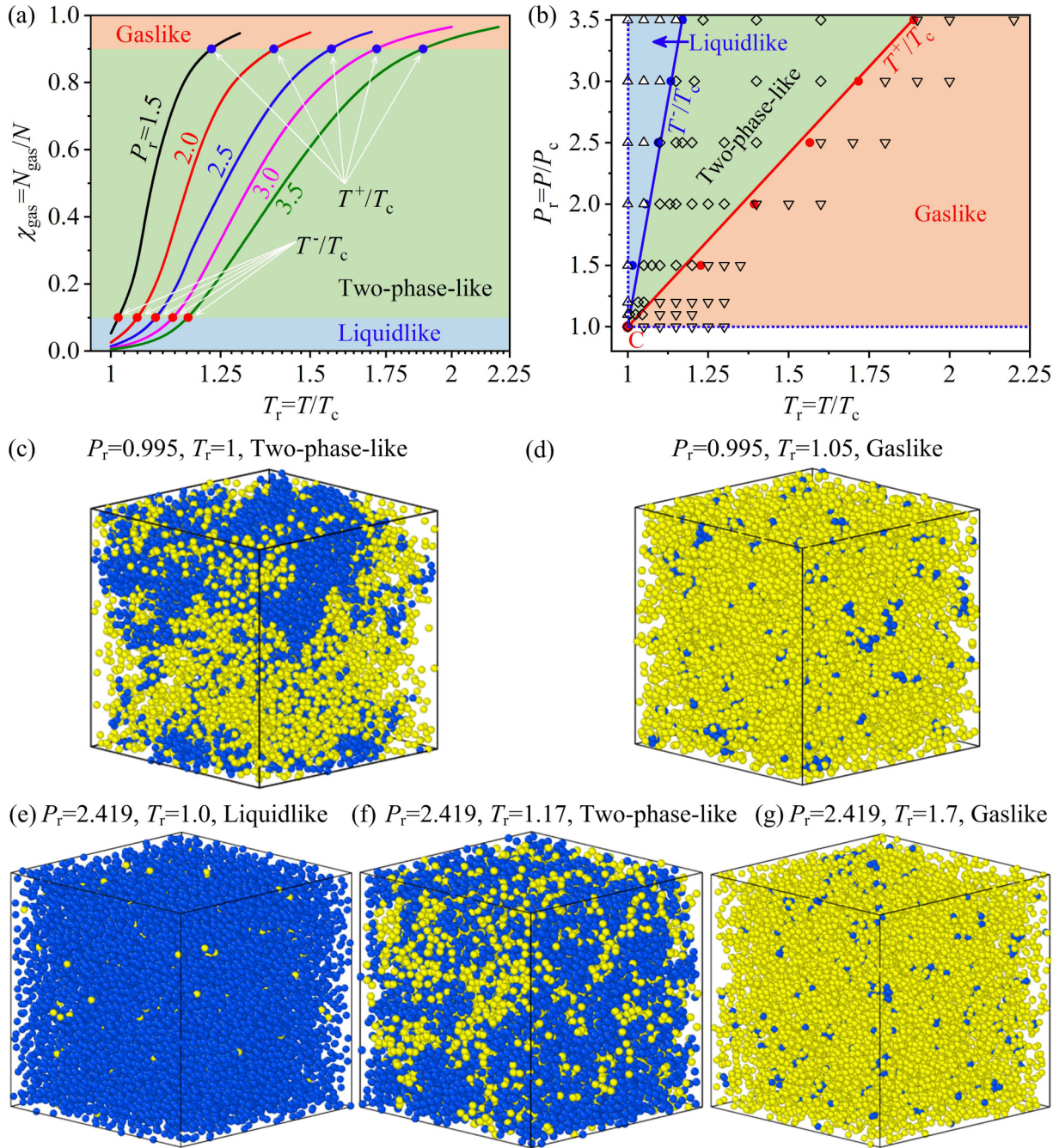


FIG. 6. The neighboring molecules method determines three regimes in a SF. (a) The vapor mass quality  $\chi_{\text{gas}}$  depends on the reduced temperature and pressure, and the LL, TPL, and GL regimes are defined by crossing the two lines of  $\chi_{\text{gas}} = 0.1$  and  $0.9$ . (b) The three-regime model in supercritical argon is interfaced with two linear transition boundaries. Three-dimensional snapshots at  $0.995P_c$ , with (c) TPL at  $T_c$  and (d) GL at  $1.05T_c$ . Snapshots at  $2.419P_c$ , with (e) LL at  $T_c$ , (f) TPL at  $1.17T_c$ , and (g) GL at  $1.7T_c$ .

occurs for  $0.1755 < \rho\sigma^3 < 0.4956$ , where liquid molecules are marked as blue and gas as yellow, as seen in Fig. 8.

**C. Radial distribution function and excess entropy**

Among the three states of solid, liquid, and gas, the gas molecules have the largest distance between neighboring particles with random motion, which is summarized as *long range disorder and short range disorder* [55,56]. The radial

distribution function  $g(r_c)$  quickly decays to 1 without obvious peaks and valleys. In contrast, liquid molecules are closely packed to yield *short range order and long range disorder* [55,56]. The ratio of first valley value  $g_{\text{min}}$  relative to the first peak value  $g_{\text{max}}$ ,  $\eta = g_{\text{min}}/g_{\text{max}}$ , has been used to study freezing and melting problems [57,58]. Here, this method is extended to determine  $T^-$  and  $T^+$ . The  $g(r_c)$  in the liquid regime has the largest oscillations but in the gas regime it has weak oscillations, which agrees with the results of Ref. [59].



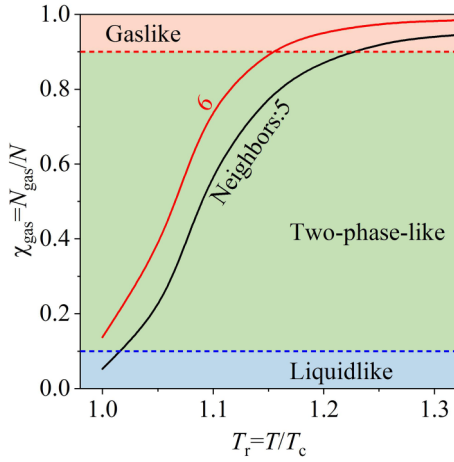


FIG. 7. The outcomes of  $\chi_{\text{gas}}$  dependent on neighboring molecules of target molecule.

The  $g(r_c)$  in the TPL regime is in between those of liquid and gas at  $1.478P_c$ , as seen in Fig. 9(a). By comparing the four panels in Fig. 10 with  $P = 1.957P_c, 2.419P_c, 2.956P_c,$  and  $3.419P_c$ , different pressures share common variation trends of  $g(r_c)$  with respect to  $r_c(\sigma)$ , but temperatures have a strong effect on  $g(r_c)$  distribution. LL displays multiple peak distribution at  $T = T_c$ , but only a single peak occurs for higher temperatures such as  $1.5T_c$  at  $1.957P_c$  and  $1.7T_c$  at  $2.419P_c$ , as seen in Figs. 10(a) and 10(b), which are consistent with those reported in Ref. [60].

The  $\eta$  curve is plotted versus the reduced temperatures in Fig. 9(b) at  $1.478P_c$ , including two linear parts and a curved part. In the lower temperature region, the curved section begins to deviate from the linear section at the point  $t_1$ , with the corresponding temperature marked as  $T^-$  at the onset pseudoboiling temperature. At the higher temperature region, the curved section begins to deviate from the linear section at the point  $t_2$ , with the corresponding temperature marked as  $T^+$  as the termination pseudoboiling temperature. The slopes of the  $\eta$  curves vary over the entire temperature range; they are

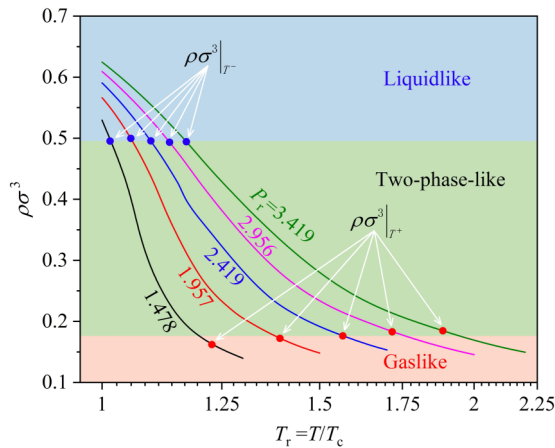


FIG. 8. Effects of reduced temperatures and pressures on the number density. The LL, TPL, and GL regimes are defined by two transition boundaries of  $\rho\sigma^3|_{T^-}$  and  $\rho\sigma^3|_{T^+}$ .

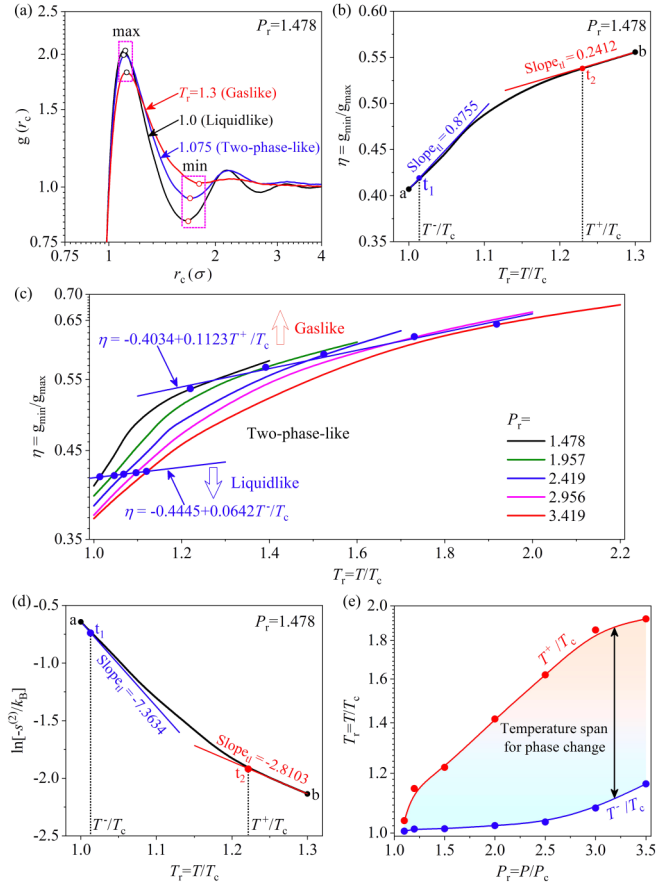


FIG. 9. Radial distribution function (RDF) and two-body excess entropy-determined transition boundaries. (a)  $g(r_c)$  function versus  $r_c$  for the three regimes at  $1.478P_c$ . (b) Three parts of the curves  $\eta = g_{\text{min}}/g_{\text{max}}$  at  $1.478P_c$ . (c) The  $\eta$  at various temperatures and pressures. (d) Three parts of the two-body excess entropy curves versus  $T_r$ . (e) Excess entropy-determined transition boundaries.

0.8755 for section  $t_1$  and 0.2412 for section  $t_2$ . We summarize the  $\eta$  curves in Fig. 9(c) at various pressures from  $1.5P_c$  to  $3.5P_c$ . Switching the  $T^-$  and  $T^+$  values at different pressures and temperatures based on Fig. 9(c) could give a regime map that includes LL, TPL, and GL, which is similar to Fig. 6(b).

We present the outcomes of  $T^-$  and  $T^+$  based on the two-body excess entropy,  $s^{(2)}$ , which characterizes the degree of ordering [42]. The two-body excess entropy is modified into a nondimensional and log form at  $1.478P_c$ , as seen in Fig. 9(d). It is noted that there is a three-part structure in supercritical argon. The two linear sections have slopes of  $-7.3634$  and  $-2.8103$  in the lower and higher temperature regions, respectively. Similar to the radial distribution function  $g(r_c)$  method shown in Fig. 9(b), the excess entropy approach yields the two transition points of  $t_1$  and  $t_2$  corresponding to  $T^-$  and  $T^+$ , respectively. Additional data for the excess entropy curves are provided in Fig. 11. These data allow us to generate the regime map to include LL, TPL, and GL in Fig. 9(e).

#### D. Comparison between different approaches

There is a saturation temperature for subcritical boiling. However, a supercritical pressure for pseudoboiling cor-

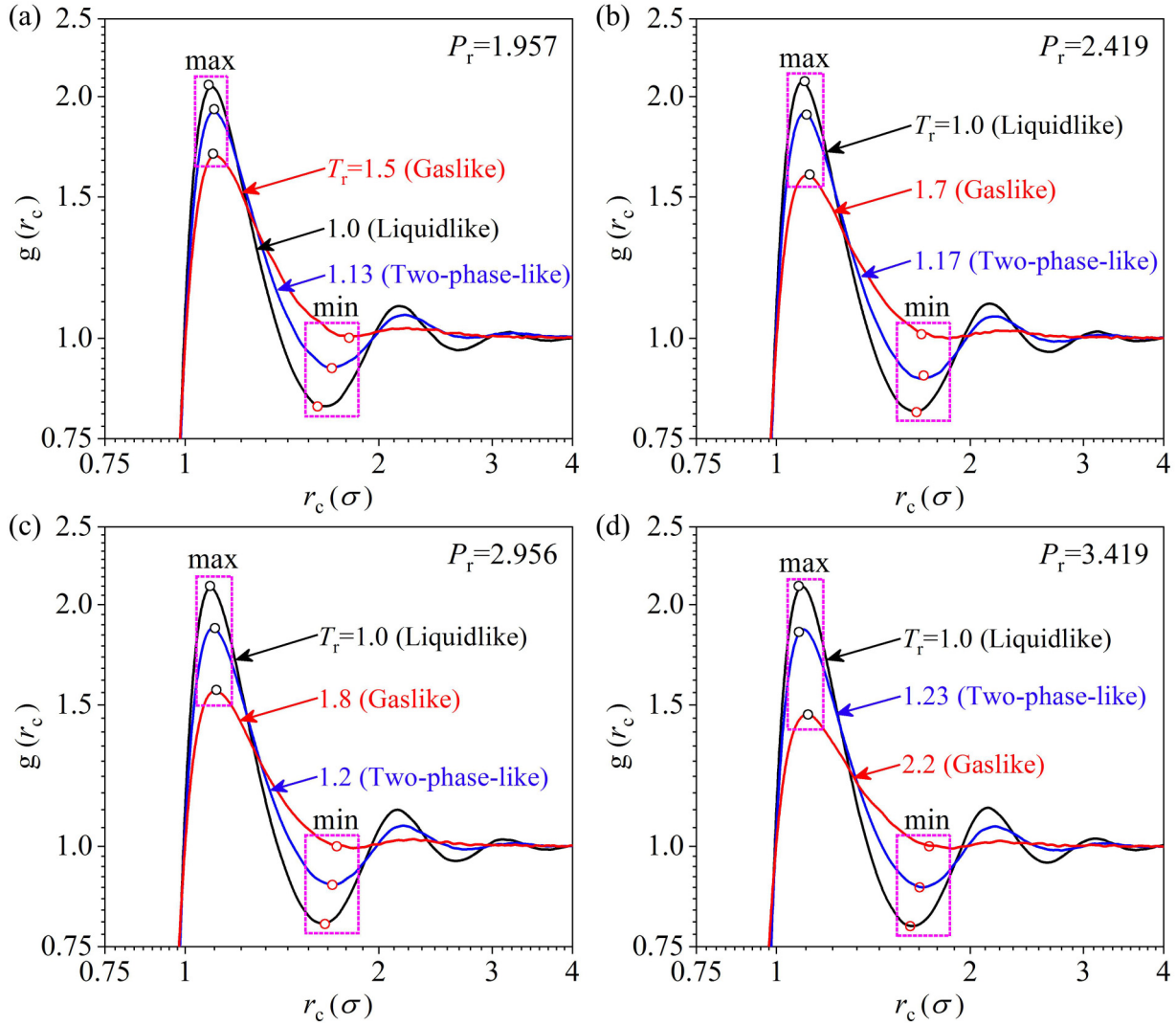


FIG. 10. Radial distribution function (RDF) at different pressures showing different responses versus  $r_c$  in three different regimes, with (a)  $P_r = 1.957$ , (b)  $P_r = 2.419$ , (c)  $P_r = 2.956$ , and (d)  $P_r = 3.419$ .

responds to a temperature interval between  $T^-$  and  $T^+$ . Figure 12(a) reconstructs the regime map to include LL, TPL, and GL based on  $T^-$  and  $T^+$  as determined using the neigh-

boring molecules,  $g(r_c)$ , excess entropy, and thermodynamic methods. These four methods are compared and summarized in Fig. 12(b) and Table II. The thermodynamically determined values are taken as the reference data for the comparison. The conclusions are as follows. (1) Perfect agreement is achieved between the four methods. More than half of the data points have relative errors of less than 2%. (2) The relative errors slightly increase with pressure, and approximately 80% of the data points have relative errors less than 5%. (3) The largest deviation occurs at  $\sim 3P_c$  but is less than 10%.

The enthalpies are plotted in Fig. 12(c) with a maximum pressure of up to  $3.5P_c$ . At subcritical pressures, the latent heat of evaporation,  $i_{lg}$ , quantifies how much energy is needed for the phase change from pure liquid to pure gas, which decreases with pressure until reaching zero at the critical pressure. Now that  $T^-$  and  $T^+$  are determined at supercritical pressures, the pseudoboiling enthalpy is defined as  $\Delta i_t = i_{T^+} - i_{T^-}$ , which reflects an integration of the specific heat ( $c_p$ ) curve in the temperature interval of  $T^-$  to  $T^+$ . A nonmonotonic increase is observed for  $\Delta i_t$  to include an initial increase rise section with  $1 < P_r < 1.6$ , a nearly hor-

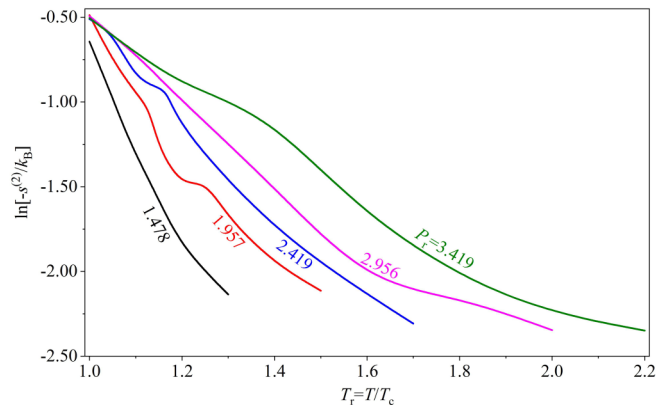


FIG. 11. Two-body excess entropies versus reduced temperatures at different reduced pressures.

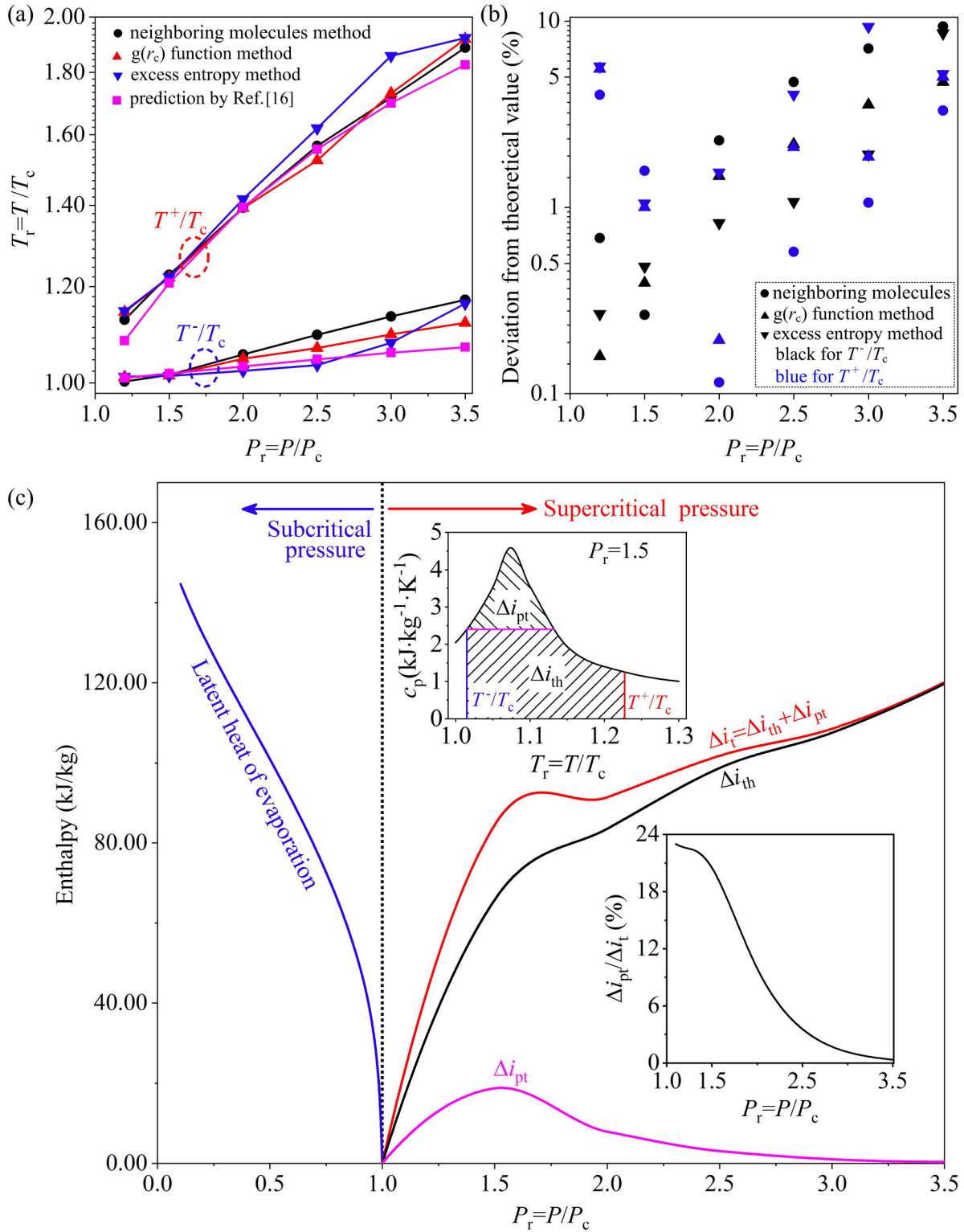


FIG. 12. Summary of the outcomes for the two transition temperatures. (a) Comparison between different approaches and (b) the error distribution. (c) Enthalpy distribution versus pressure when interfaced at the critical pressure.

horizontal section with  $1.6 < P_r < 2.0$ , and a second increase section with  $P_r > 2$ . Decoupling  $\Delta i_t$  into two parts yields  $\Delta i_t = \Delta i_{pt} + \Delta i_{th}$ , where  $\Delta i_{pt}$  is used to overcome intermolecular attraction, which is an excess energy to enlarge the distance between neighboring molecules and is similar to the function of latent heat of evaporation in subcritical boiling,

and  $\Delta i_{th}$  is used to increase the temperature only. We note that for subcritical phase change,  $\Delta i_{th} = 0$  exists due to the constant temperature evaporation. The  $\Delta i_{pt}/\Delta i_t$  is defined to characterize the ratio of the energy to overcome intermolecular attraction relative to the total energy for pseudoboiling. The  $\Delta i_{pt}$  accounts for  $\sim 22\%$  of the total pseudoboiling en-

TABLE II.  $T^-$  and  $T^+$  determined using various methods and comparisons between them.

(a) $T^-/T_c$ values and their errors related to theoretical values				
$P_r = P/P_c$	Decided by neighboring molecules method and error (%)	Decided by $g(r_c)$ method and error (%)	Decided by excess entropy method and error (%)	Decided by thermo dynamic method
$P_r = 1.02$	–	1.00157	1.00349	–
1.2	1.0023, 0.684	1.0108, 0.159	1.0119, 0.268	1.0092
1.5	1.015, 0.265	1.0137, 0.393	1.0128, 0.481	1.0177
2.0	1.055, 2.288	1.0466, 1.474	1.0229, 0.824	1.0314
2.5	1.095, 4.715	1.0682, 2.181	1.0342, 1.071	1.0454
3.0	1.134, 7.123	1.0962, 3.552	1.0790, 1.927	1.0586
3.5	1.170, 9.366	1.1202, 4.711	1.1619, 8.609	1.0698
(b) $T^+/T_c$ values and their errors related to theoretical values				
$P_r = P/P_c$	Decided by neighboring molecules method and error (%)	Decided by $g(r_c)$ method and error (%)	Decided by excess entropy method and error (%)	Decided by thermo dynamic method
$P_r = 1.02$	–	1.11890	1.08018	–
1.2	1.127, 4.024	1.1434, 5.538	1.1454, 5.723	1.0834
1.5	1.227, 1.572	1.2201, 1.002	1.2217, 1.051	1.2080
2.0	1.393, 0.115	1.3919, 0.194	1.4161, 1.542	1.3946
2.5	1.566, 0.578	1.5243, 2.100	1.6199, 4.040	1.5570
3.0	1.717, 1.059	1.7307, 1.866	1.8574, 9.323	1.6990
3.5	1.887, 3.312	1.9182, 5.021	1.9216, 5.207	1.8265

ergy for  $P_r < 1.6$ , then decays with increase of pressures, and becomes unimportant for  $P_r > 3$ . Hence, we conclude the important role of  $\Delta i_{pt}$  to overcome intermolecular attraction, which is a core mechanism to form the bubblelike regime in SFs.

### E. Bubblelike regime in SF

The grid marking technique is developed to determine the fluid phase (liquid or gas) that is occupied by each grid with a cell size of  $1\sigma \times 1\sigma$  and a  $10\sigma$  thickness in the  $y$  direction (see Fig. 13). The MD simulation outcomes yield  $\rho\sigma^3$  for each grid. Based on Fig. 8, each grid is filled with either blue for liquid or white for gas with  $\rho\sigma^3 > 0.4956$  and  $\rho\sigma^3 < 0.1755$ , respectively. The gray color in a grid is given for  $0.1755 <$

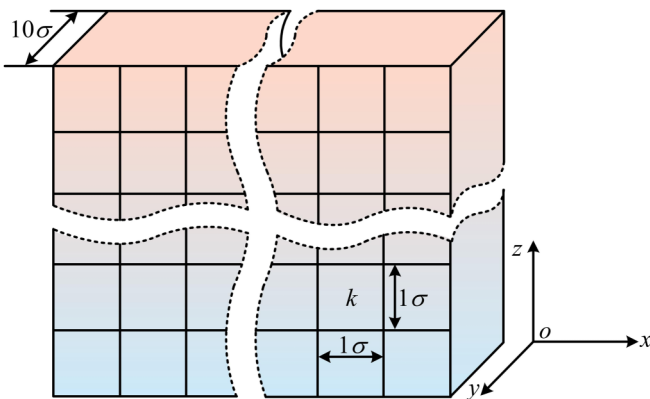


FIG. 13. The grid marking method to decide the density for the judgment whether a grid is occupied by LL, transition, or GL in such a grid.

$\rho\sigma^3 < 0.4956$ . Three pressures of  $1.064P_c$ ,  $1.155P_c$ , and  $1.478P_c$  are paid attention to here. The continuous phase is liquidlike for  $T \leq T^-$ , but the continuous phase is gaslike for  $T \geq T^+$  [see Fig. 14(a)].

For the three groups of combined parameters of  $P_r$  and  $T_r$  given in Fig. 14(b) (see Supplemental Material [54] for a two-dimensional (2D) movie), voids are observed in the eTPL regime. These voids are  $\sim 10\sigma$  in size and have a curved interface. To understand the voids shown in Fig. 14(b), the snapshot for  $1.046P_c$  and  $1.0056T_c$  is enlarged in Fig. 15 focusing on a void. The void has the following characteristics. First, the void contains sparsely populated molecules, but outside the void there are densely populated molecules. It cannot say that the void is a “vacuum.” The void has a gaslike density with  $\rho\sigma^3 < 0.1755$ , but outside of the void there is a liquidlike density with  $\rho\sigma^3 > 0.4956$ . Second, the void has a curved interface. These two features conclude the bubblelike pattern in the TPL regime, which is analogous to bubbles in subcritical pressure. A bubblelike structure occurs for pressures of  $\sim 1.5P_c$  and even higher. It is impossible to arrange uniformly distributed molecules in SF. A Bubblelike structure helps to minimize the free energy of the SF system, satisfying the minimum energy principle. The bubblelike structure in the TPL regime needs further investigation.

### F. Nonlinear analysis of SF

Nonlinear analysis has been widely applied in biology, weather forecasting, mechanical damping, electronic signals, and complex fluids [61,62]. Multiphase fluids have been investigated using nonlinear analysis [63]. Because most multiphase systems display chaotic behavior, we explore whether SFs also display chaotic features. If the answer is *yes*, the



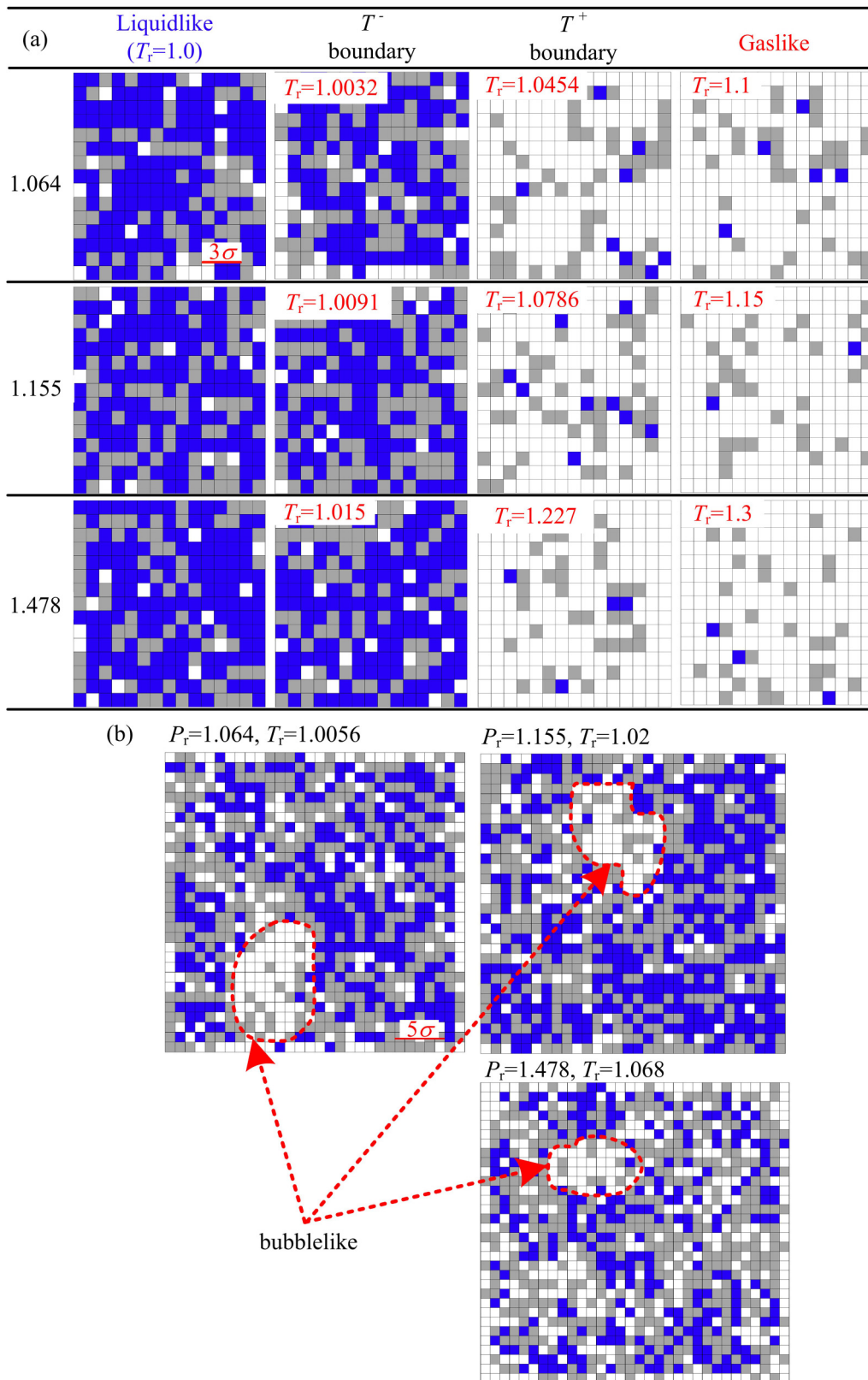


FIG. 14. Snapshots showing the phase distributions at a layer thickness of  $10\sigma$  in the  $y$  direction. (a) Phase distributions in the LL and GL regimes and at the two transition boundaries, and (b) the TPL regime showing a bubblelike region.

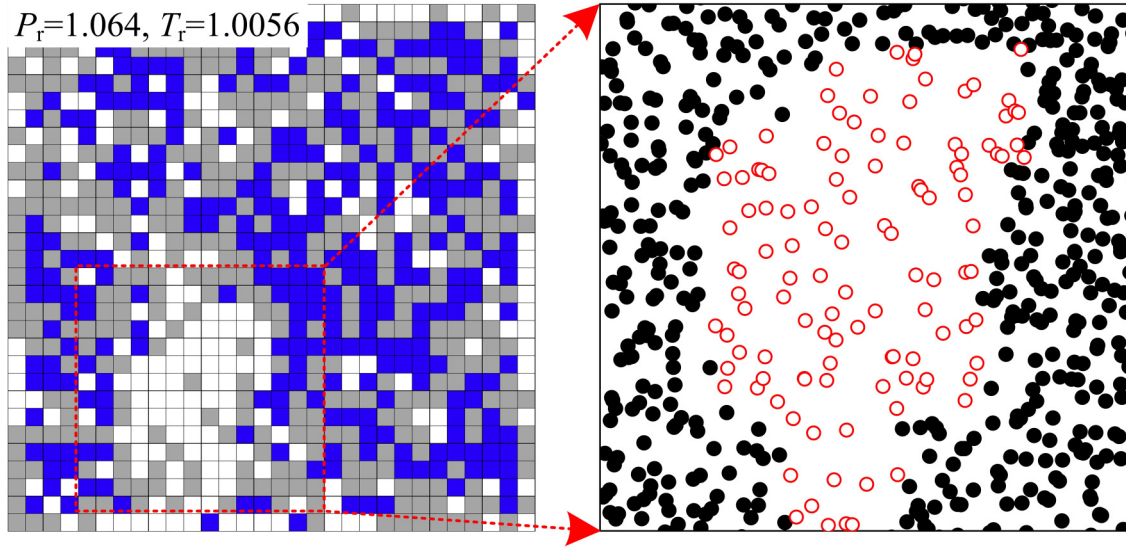


FIG. 15. The phase and molecule distributions at  $1.064P_c$  and  $1.0056T_c$ .

evidence of bubblelike related two-phase structure will be enhanced for SFs. We select the centered  $10\sigma$  thickness in the  $y$  direction and plot the time series  $\rho\sigma^3$  in Fig. 16(a), in which three regimes, LL at  $T_c$ , TPL at  $1.068T_c$ , and GL at  $1.3T_c$ , are demonstrated. We note the constant fluid density in the whole box. In this paper, 1000 data samples in 5 ns after the system equilibrium were chosen for nonlinear analysis. Density fluctuations in the  $10\sigma$  thickness reflect the mass exchange between such layer and its neighboring layers. Even though outcomes are only presented at  $1.478P_c$ , the time series signals at other supercritical pressures are similar to those at  $1.478P_c$ . The square root error  $e_s$  is

$$e_s = \sqrt{\sum_{f=1}^{N_s} \left( \frac{\rho\sigma^3|_f - \rho\sigma^3|_{ave}}{\rho\sigma^3|_{ave}} \right)^2 / N_s}, \quad (13)$$

where  $N_s$  is the total number of data samples,  $f$  is the  $f$ th time step, and  $ave$  is the average value. Evidenced by larger square root error in the TPL regime, we conclude there are stronger oscillations in the TPL regime than in the LL and GL regimes. We identify different responses of correlation dimensions at different structures, as seen in Figs. 16(b) and 16(c). In the LL and GL regimes, correlation dimensions show monotonic rises versus embedding dimensions to display random behavior. In the TPL regime with increase of embedding dimensions, correlation dimensions rise, attain the maximum, and then decrease. At  $1.478P_c$  and  $1.121T_c$ , the peak point is located at the embedding dimension of 8 and the correlation dimension of 4.7104, concluding that SF at this state should be described using at least five independent parameters, but the number of independent parameters should be smaller than nine. The largest Lyapunov exponent is an important parameter. Especially, in a fluid system, the positive and negative Lyapunov exponents refer to chaotic and random behavior, respectively. Figure 16(d) shows the Lyapunov exponents versus the reduced temperature at  $1.478P_c$ , showing chaotic behavior corresponding to a two-phase-like (TPL) regime, which is similar to a two-phase mixture in subcritical

pressure. The random behavior corresponds to a liquidlike (LL) regime at lower temperature and gaslike (GL) at higher temperature. The attractor pattern is important to classify the dynamic features of a system (see Fig. 17). Attractor portraits in the LL and GL regimes display irregular patterns, with the attractor converging towards the portrait center. The internal structure of the attractor patterns cannot be seen, indicating random behavior in LL and GL fluids. However, the TPL regime has a different attractor pattern, which is formed by superimposing a set of line rings. Fine internal structures can be seen, belonging to a chaotic dynamic which is similar to two-phase structure in subcritical pressure.

In summary, our work demonstrates that a supercritical fluid can be a mixture of LL and GL. The multiphase fluid theory in subcritical pressure can be introduced to deal with complicated SFs. The similarity between subcritical pressure and supercritical pressure is a prospective research direction for SFs. To establish such a connection, various parameters are to be determined. Here, we analogize the pseudoboiling enthalpy  $\Delta i_t$  in supercritical pressure to the latent heat of evaporation in subcritical pressure. The temperature interval between  $T^-$  and  $T^+$  is analogized to the saturation temperature in subcritical pressure. To introduce the multiphase theory framework, some parameters have not been decided yet, but should be done in the future. Physical parameters such as viscosity, thermal conductivity, and specific heat should be defined for GL and LL, respectively. The two transition temperatures  $T^-$  and  $T^+$  may be the temperatures to determine the parameters at the liquid state and gas state, respectively. Besides, there are several nondimensional parameters in subcritical multiphase systems, including the Bond number, Weber number, and capillary number [52]. These nondimensional parameters are also needed in supercritical pressure, representing the importance of one force relative to another. Both numerical simulations and experimental techniques widely applied in subcritical pressure are to be introduced in supercritical pressure. Our work opens an interesting research direction to introduce the multiphase theory framework to the supercritical domain, not only enhancing

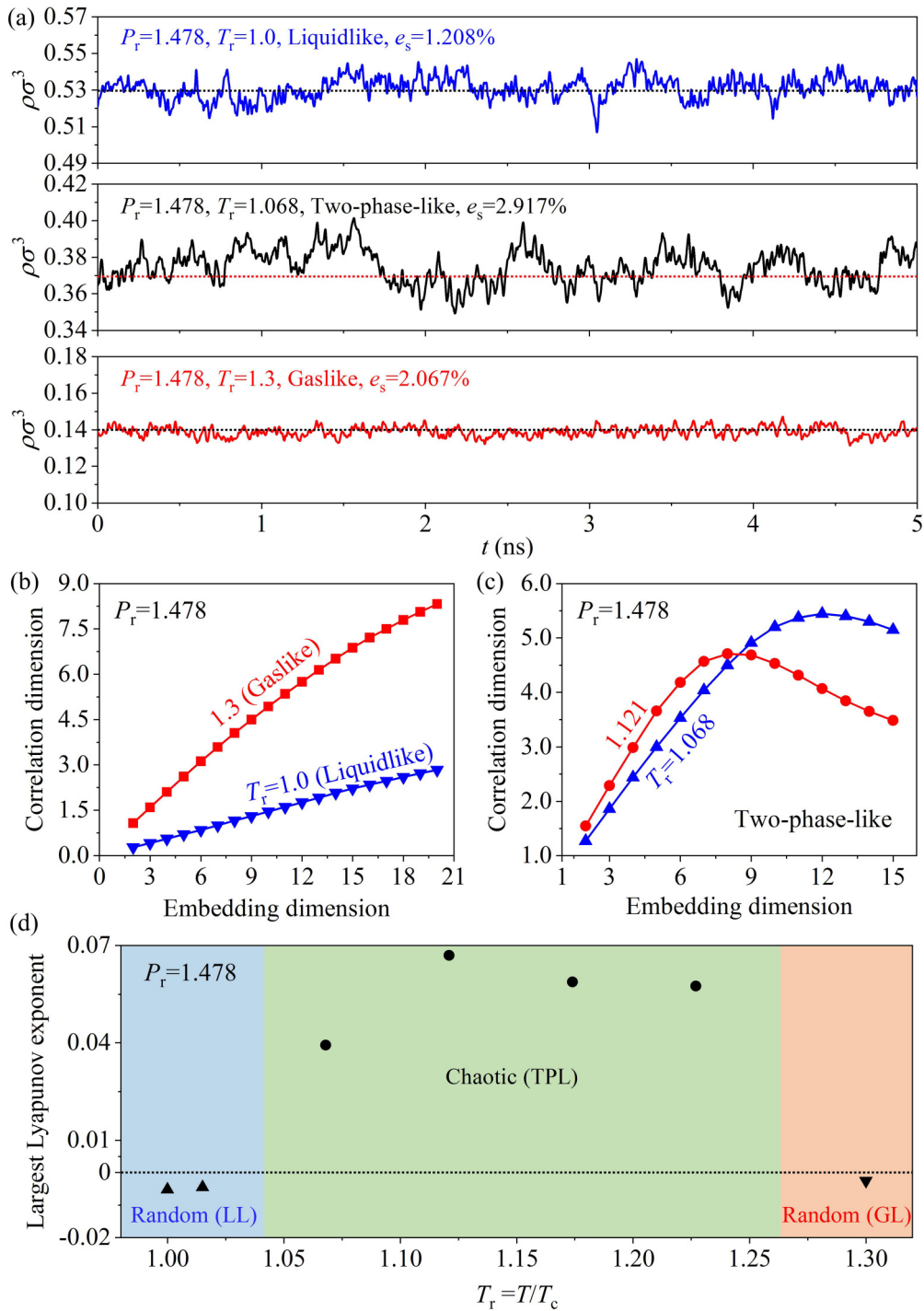


FIG. 16. Nonlinear analysis of the SF. (a) Density fluctuations for a  $10\sigma$  layer thickness in the  $y$  direction showing larger oscillations in the TPL regime. (b)–(c) Correlation dimensions versus the embedding dimensions showing an increasing trend for LL and GL, but saturation for TPL. (d) Nonlinear characteristics showing randomness in the LL and GL regimes and chaotic behavior in the TPL regime, which is similar to the two-phase regime at subcritical pressures.

the understanding of SFs, but also improving design accuracy for advanced energy systems.

#### IV. CONCLUSIONS

SFs are a natural phenomenon and can find various applications in industries. The SF is regarded as a homogeneous and

single-phase fluid (which is documented in textbooks [10]), displays a sharp transition between LL and GL by crossing the Widom line [19,20,22], or is divided into three regimes by two transition temperatures  $T^-$  and  $T^+$  based on enthalpy analysis [16]. Because at this stage, fluid structures in SFs are not fully understood, the predicted thermal performance greatly deviates from experimental data, limiting

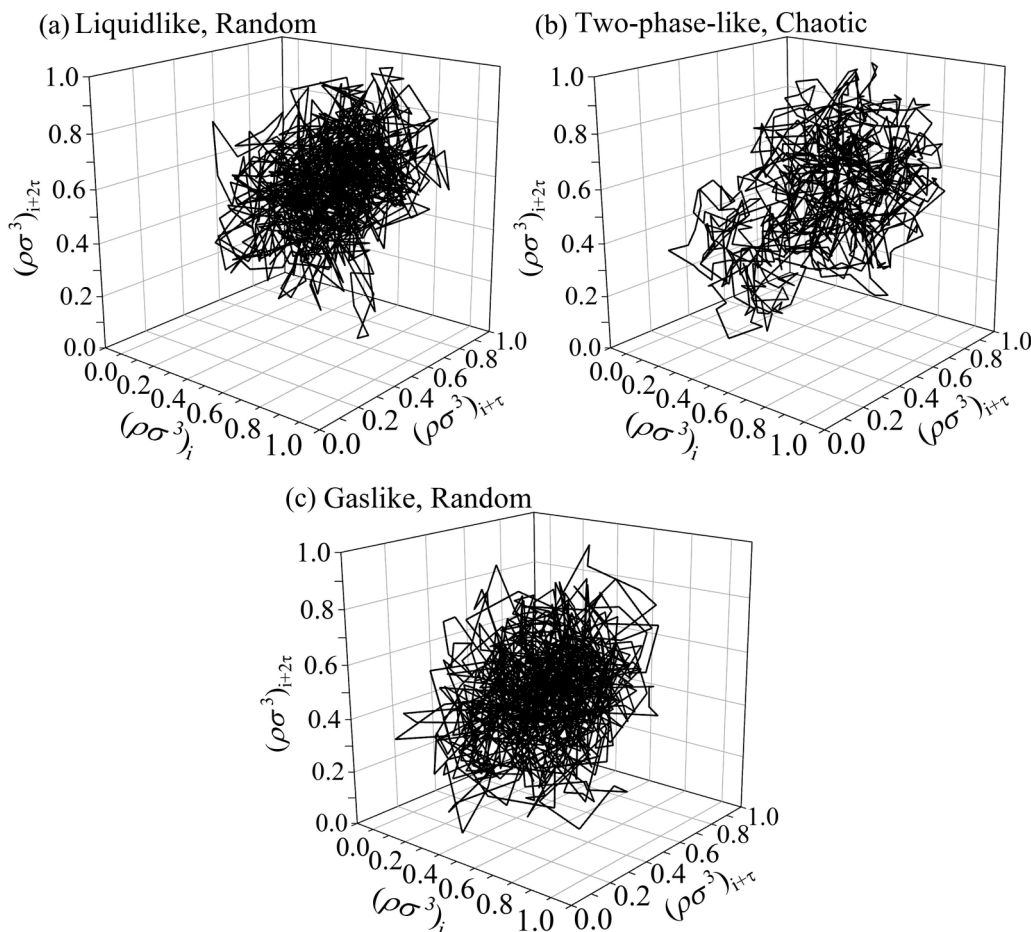


FIG. 17. Attractor patterns with (a), (c) for random behavior in the LL and GL regimes, and (b) chaotic behavior in the TPL regime.

large scale utilizations of supercritical technologies in energy systems and synthesis of functional nanomaterials [12,18]. In this paper, MD simulations with argon fluid were simulated focusing on the phase distribution in SF. Periodic boundary conditions were applied on all the surfaces of a simulation box including 10976 argon atoms. The onset pseudoboiling temperature  $T^-$  and termination pseudoboiling temperature  $T^+$  were evaluated using the neighboring molecules method, the radial distribution function (RDF) method, and the two-body excess entropy method, based on MD simulation results. By verifying phase distribution in different pressures and temperatures, we show that the two transition temperatures divide the whole phase diagram into three regimes, LL, TPL, and GL, instead of the sharp transition between LL and GL

reported in the literature. Most importantly, the TPL regime is found to contain voids and surrounding liquids. The observed voids have gas densities inside and a curved interface. Hence, voids are said to be bubblelike. We further explain why the term “bubblelike” is reasonable in the supercritical domain, by making a link with the subcritical domain. Our work highlights important multiphase features of the SF including the bubblelike feature. Nonlinear analysis based on time series density data supports the multiphase feature of the SF.

#### ACKNOWLEDGMENT

This work was supported by the National Natural Science Foundation of China (Grant No. 51821004).

- [1] B. Berche, M. Henkel, and R. Kenna, *J. Phys. Studies* **13**, 3201 (2009).
- [2] J. Xu, E. Sun, M. Li, H. Liu, and B. Zhu, *Energy* **157**, 227 (2018).
- [3] W. H. Stein and R. Buck, *Sol. Energy* **152**, 91 (2017).
- [4] H. Pinkowska, P. Wolak, and A. Zlocinska, *Chem. Eng. J.* **187**, 410 (2012).

- [5] F. van Rantwijk and R. A. Sheldon, *Chem. Rev.* **107**, 2757 (2007).
- [6] L. Qian, S. Wang, D. Xu, Y. Guo, X. Tang, and L. Wang, *Water Res.* **89**, 118 (2016).
- [7] K. P. Johnston and P. S. Shah, *Science* **303**, 482 (2004).
- [8] M. J. Cocero, A. Cabeza, N. Abad, T. Adamovic, L. Vaquerizo, C. M. Martinez, and M. V. Pazo-Cepeda, *J. Supercrit. Fluids* **133**, 550 (2018).



- [9] A. A. Peterson, F. Vogel, R. P. Lachance, M. Froeling, M. J. Antal, Jr., and J. W. Tester, *Energ. Environ. Sci.* **1**, 32 (2008).
- [10] Y. A. Cengel and M. A. Boles, *Thermodynamics: An Engineering Approach* (McGraw-Hill, New York, 2009).
- [11] S. Zhang, X. Xu, C. Liu, X. Liu, and C. Dang, *Appl. Therm. Eng.* **157**, 113687 (2019).
- [12] B. Zhu, J. Xu, C. Yan, and J. Xie, *Int. J. Heat Mass Transfer* **148**, 119080 (2020).
- [13] J. P. Holman, S. N. Rea, and C. E. Howard, *Int. J. Heat Mass Transfer* **8**, 1095 (1965).
- [14] K. K. Knapp and R. H. Sabersky, *Int. J. Heat Mass Transfer* **9**, 41 (1966).
- [15] J. Wang, H. Li, S. Yu, and T. Chen, *Int. J. Multiphase Flow* **37**, 769 (2011).
- [16] D. T. Banuti, *J. Supercrit. Fluids* **98**, 12 (2015).
- [17] F. Maxim, K. Karalis, P. Boillat, D. T. Banuti, and C. Ludwig, *Adv. Sci.* **8**, 2002312 (2020).
- [18] F. Maxim, C. Contescu, P. Boillat, B. Niceno, and C. Ludwig, *Nat. Commun.* **10**, 4114 (2019).
- [19] P. Gallo, D. Corradini, and M. Rovere, *Nat. Commun.* **5**, 5806 (2014).
- [20] G. G. Simeoni, T. Bryk, F. A. Gorelli, M. Krisch, G. Ruocco, M. Santoro, and T. Scopigno, *Nat. Phys.* **6**, 503 (2010).
- [21] A. S. Raman, H. Li, and Y. C. Chiew, *J. Chem. Phys.* **148**, 014502 (2018).
- [22] P. F. Mcmillan and H. E. Stanley, *Nat. Phys.* **6**, 479 (2010).
- [23] D. T. Banuti, M. Raju, and M. Ihme, *J. Supercrit. Fluids* **165**, 104895 (2020).
- [24] D. Bolmatov, V. V. Brazhkin, and K. Trachenko, *Nat. Commun.* **4**, 2331 (2013).
- [25] M. Raju, D. T. Banuti, P. C. Ma, and M. Ihme, *Sci. Rep.* **7**, 3027 (2017).
- [26] M. Y. Ha, T. J. Yoon, T. Tlusty, Y. Jho, and W. B. Lee, *J. Phys. Chem. Lett.* **9**, 1734 (2018).
- [27] J. Tamba, T. Takahashi, T. Ohara, and T. Aihara, *Exp. Therm. Fluid Sci.* **17**, 248 (1998).
- [28] K. Nishikawa, T. Ito, and H. Yamashita, *J. Heat Transfer* **95**, 187 (1973).
- [29] N. Yoshii and S. Okazaki, *Fluid Phase Equilib.* **144**, 225 (1998).
- [30] N. Yoshii and S. Okazaki, *J. Chem. Phys.* **107**, 2020 (1997).
- [31] K. Ghosh and C. V. Krishnamurthy, *Phys. Rev. E* **97**, 012131 (2018).
- [32] D. Bolmatov, M. Zhernenkov, D. Zav'Yalov, S. N. Tkachev, A. Cunsolo, and Y. Q. Cai, *Sci. Rep.* **5**, 15850 (2015).
- [33] H. J. C. P. Berendsen, J. Postma, W. Gunsteren, A. D. Dinola, and J. R. Haak, *J. Chem. Phys.* **81**, 3684 (1984).
- [34] D. C. Rapaport, *The Art of Molecular Dynamics Simulation* (Cambridge University Press, Cambridge, 2004).
- [35] S. Nosé, *J. Chem. Phys.* **81**, 511 (1984).
- [36] W. G. Hoover, *Phys. Rev. A* **31**, 1695 (1985).
- [37] S. Plimpton, *J. Comput. Phys.* **117**, 1 (1995).
- [38] P. R. ten Wolde and D. Frenkel, *J. Chem. Phys.* **109** (1998).
- [39] J. Losey and R. J. Sadus, *Phys. Rev. E* **100**, 052132 (2019).
- [40] D. T. Banuti, M. Raju, P. C. Ma, M. Ihme, and J.-P. Hickey, in: *55th AIAA Aerospace Sciences Meeting*, no. 2017-1106, Grapevine, Texas, 2017.
- [41] S. Han, *Phys. Rev. E* **84**, 051204 (2011).
- [42] T. M. Truskett, S. Torquato, and P. G. Debenedetti, *Phys. Rev. E* **62**, 993 (2000).
- [43] Y. Song and J. Xu, *Int. J. Heat Mass Transfer* **52**, 2932 (2009).
- [44] G. Cammarata, A. Fichera, and A. Pagano, *Int. Commun. Heat Mass Transfer* **27**, 1077 (2000).
- [45] H. G. Schuster and W. Just, *Deterministic chaos. An introduction* (Wiley-VCH, Berlin, 2005).
- [46] H. S. Kim, R. Eykholt, and J. D. Salas, *Phys. D (Amsterdam, Neth.)* **127**, 48 (1999).
- [47] J. Qu, H. Wu, P. Cheng, and X. Wang, *Int. J. Heat Mass Transfer* **52**, 3481 (2009).
- [48] M. Allen and D. Tildesley, *Computer Simulation of Liquids* (Oxford University Press, Oxford, UK, 2017).
- [49] I. Skarmoutsos and J. Samios, *J. Phys. Chem. B* **110**, 21931 (2006).
- [50] F. Xing, J. Xu, J. Xie, H. Liu, Z. Wang, and X. Ma, *Int. J. Multiphase Flow* **71**, 98 (2015).
- [51] J. Wedekind and D. Reguera, *J. Chem. Phys.* **127**, 154516 (2007).
- [52] V. P. Carey, *Liquid-Vapor Phase-Change Phenomena: An Introduction to the Thermophysics of Vaporization and Condensation Processes in Heat Transfer Equipment* (Taylor & Francis, Bristol, PA, 2020).
- [53] J. Julin, M. Shiraiwa, R. E. H. Miles, J. P. Reid, U. Poschl, and I. Riipinen, *J. Phys. Chem. A* **117**, 410 (2013).
- [54] See Supplemental Material at <http://link.aps.org/supplemental/10.1103/PhysRevE.104.014142> for 3D videos corresponding to Figs. 6(c)–6(g) and 2D videos corresponding to Fig. 14(b).
- [55] Y. Waseda, *The Structure of Noncrystalline Materials: Liquids and Amorphous Solids* (McGraw-Hill International Book, New York, 1980).
- [56] J. L. Barrat and J. P. Hansen, *Basic Concepts for Simple and Complex Liquids* (Cambridge University Press, 2003)..
- [57] H. R. Wendt and F. F. Abraham, *Phys. Rev. Lett.* **41**, 1244 (1978).
- [58] F. F. Abraham, *J. Chem. Phys.* **72**, 359 (1980).
- [59] D. Bolmatov, V. V. Brazhkin, Y. D. Fomin, V. N. Ryzhov, and K. Trachenko, *J. Chem. Phys.* **139**, 234501 (2013).
- [60] D. T. Banuti, M. Raju, and M. Ihme, *Cent. Turbul. Res. Annu. Res. Brifs* **2017**, 165 (2017).
- [61] P. Sundararajan and A. D. Stroock, *Annu. Rev. Chem. Biomol. Eng.* **3**, 473 (2012).
- [62] E. Bradley and H. Kantz, *Chaos* **25**, 097610 (2015).
- [63] S. F. Wang, R. Mosdorf, and M. Shoji, *Int. J. Heat Mass Transfer* **46**, 1519 (2003).